Research Article

Analysis of the effect of dielectric losses on the bandwidth of microstrip patch antenna in stacked geometry and modelling

Boualem Mekimah[1] · **Abderraouf Messai**[1] · **Abdelkrim Belhedri**[1]

Received: 12 December 2019 / Accepted: 18 February 2020 / Published online: 27 March 2020

Abstract
This paper presents a detailed analysis involving dielectric materials, by giving rigorous formulations including losses within nonmagnetic dielectric materials. The choice of these latter has shown a thorough attention in designing microstrip patch antenna (MPA), since they have significant correlation with the MPA performance. This study aims to analyze dielectric losses effect on MPA bandwidth in stacked patch geometry, including two rectangular patches etched on two layers, rather than single-layer geometry. The paper provides detailed formulations of rigorous analysis method, in which transfer matrices at boundaries are given regarding the studied case. Numerical results are presented and agreed with previous findings, where the dielectric losses show positive effect on both lower and upper bandwidths of the stacked patch geometry. The present study therefore provides additional evidence to the losses within low cost dielectric materials.

Keywords Microstrip patch antenna · Dielectric materials · Dielectric losses · Dielectric permittivity · Quality factor

1 Introduction

Dielectric materials state can be either solid, liquid, or gas. The most commonly used state, in electrical engineering, is the solid one. An ideal dielectric material is a medium that does not contain any free electric charges which can move from molecule to molecule [1–3]. It is sometimes called electrical insulation. In fact, a dielectric material has bound charges which can move only inside the molecules of this latter, when an electric field is applied. This field interacts with electrostatic dipoles of atoms or molecules. This interaction leads to the creation of a polarization related to the applied field, by the so-called electric susceptibility [4, 5].

The origin of losses, within a dielectric material, is: first, because of certain conductivity σ leading to an electric current density J. This current is in phase with the applied electric field. This leads to an energy loss modeled by σ/ω ratio. Second, losses due to damping of vibrating dipole moments that can be modeled by ε'' [4, 5].

Dependence, on both temperature and frequency, of both the dielectric constant (DK) and the dissipation factor (DF) has been already reported in many research papers [1, 6–13]. However, DK and DF in datasheets are average values (typical values).

In [14], the negative effect, on the radiation efficiency of both the magnetic loss tangent and the dielectric loss tangent, is investigated, in single-layer rectangular patch geometry using full-wave simulations, where they show positive impact on the antenna bandwidth.

The author in [15] showed how the miniaturization is achieved by the use of the magnetodielectric materials ($\mu_r > 1, \varepsilon_r > 1$) in a rectangular patch geometry using transmission line analysis.

The magnetodielectric material is also used for achieving antenna miniaturization like in [16] using both full-wave

✉ Boualem Mekimah, boualem.mekimah@emt.inrs.ca; b_mekimah@umc.edu.dz | [1]Department of Electronics, University of Frères Mentouri Constantine 1, 25000 Constantine, Algeria.

simulations and transmission line model. The author studied the effect of substrate height on the bandwidth, as well as the effect of magnetic loss tangent on radiation efficiency, which showed negative impact.

The magnetodielectric material effect on MPA radiation efficiency and on bandwidth is investigated in [17] using rectangular cavity model, in which radiation efficiency is negatively affected by the relative permittivity (ε_r), unlike the relative permeability (μ_r) which shows positive impact on radiation efficiency. The same paper [17] confirms the negative impact on radiation efficiency of both magnetic loss tangent and dielectric loss tangent in the same manner.

Some other works like in [18, 19] focused on the enhancement of dielectric proprieties to meet antenna miniaturization, as well as, to enhance radiation efficiency by reducing dielectric losses. Alternatively, this can be achieved by generating novel dielectric proprieties with respect to the conventional ones.

Although extensive research has been carried out on losses within dielectric materials, the investigation of dielectric losses effect on MPA performance beyond the single-layer geometry, using alternative full-wave method, is crucially important. The stacked patches antenna geometry is considered to be more general compared to the single-layer geometries as in [14–17], where the three different geometries are possible: simple patch geometry, superstrate geometry, and stacked patch geometry.

This work focuses on modeling and analyzing losses within nonmagnetic dielectric materials ($\mu_r = 1$) in stacked patch geometry, which they have low cost compared to the magnetodielectric materials [14–17]. The effect of dielectric losses on both lower and upper bandwidths, as well as on quality factors, is investigated in this paper. The transfer matrices at boundaries are developed as a function of dielectric proprieties including dielectric losses. Numerical results are found, based on four different substrates having the same dielectric constant (ε_r) with different dissipation factors (tanδ).

The paper is organized as follows: In the second section, the studied antenna geometry is illustrated, in which the antenna operates efficiently in dual frequency band at 2.44 GHz and 3.48 GHz. Theory and analysis are well presented in the third section. A computational study of dielectric losses effect, on the stacked patch antenna performance, is realized and discussed in the fourth section. Concluding remarks are given in the last section.

2 Antenna design

The stacked patch antenna is considered as a more general configuration, to study dielectric losses, with respect to the basic single-layer geometry. The studied structure, as shown in Fig. 1, is composed of two rectangular patches, etched on two identical and isotropic dielectric materials having the same height, $h = 1.6$ mm. The bottom patch size is $w_1 \times l_1 = 22 \times 28$ mm^2 and $w_2 \times l_2 = 22 \times 21.25$ mm^2 is the top patch size. The antenna operates efficiently in dual frequency band at 2.44 GHz and 3.48 GHz.

These frequencies are preliminary calculated using transmission line model, corresponding to the rectangular patch [20, 21].

3 Theory and analysis

Among rigorous methods, the method of moments has a large number of attractive features, including high accuracy and low complexity with respect to the other rigorous methods.

In the present section, three subsections are considered, where the vector Hankel transform is used, to reduce x and y variables. Computations are performed using both FORTRAN and MATLAB tools.

3.1 Calculation of Green Dyads in vector Hankel transform domain

The transverse electric field must be zero on perfect conductors. On the ground plane, we have

$$\tilde{\boldsymbol{E}}_1\left(\boldsymbol{k}_s, \boldsymbol{z}_0^+\right) = 0 \tag{1}$$

where $\boldsymbol{k}_s = k_x\hat{\boldsymbol{x}} + k_y\hat{\boldsymbol{y}}$ is the vector Hankel transform of $\boldsymbol{r}_s = x\hat{\boldsymbol{x}} + y\hat{\boldsymbol{y}}$.

Taking into account the boundary conditions, at different interfaces, for both electric and magnetic fields,

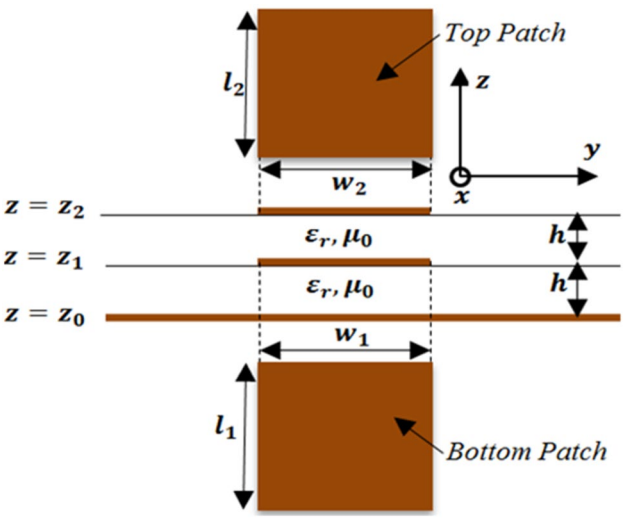

Fig. 1 Geometry of the studied antenna

$$\begin{bmatrix} \tilde{\boldsymbol{E}}_2(\boldsymbol{k}_s, z_1^+) \\ \tilde{\boldsymbol{H}}_2(\boldsymbol{k}_s, z_1^+) \end{bmatrix} = \overline{\boldsymbol{T}}_1 \begin{bmatrix} \tilde{\boldsymbol{E}}_1(\boldsymbol{k}_s, z_0^+) \\ \tilde{\boldsymbol{H}}_1(\boldsymbol{k}_s, z_0^+) \end{bmatrix} - \begin{bmatrix} 0 \\ \boldsymbol{J}(z_1) \end{bmatrix} \tag{2}$$

$$\begin{bmatrix} \tilde{\boldsymbol{E}}_3(\boldsymbol{k}_s, z_2^+) \\ \tilde{\boldsymbol{H}}_3(\boldsymbol{k}_s, z_2^+) \end{bmatrix} = \overline{\boldsymbol{T}}_2 \begin{bmatrix} \tilde{\boldsymbol{E}}_2(\boldsymbol{k}_s, z_1^+) \\ \tilde{\boldsymbol{H}}_2(\boldsymbol{k}_s, z_1^+) \end{bmatrix} - \begin{bmatrix} 0 \\ \boldsymbol{J}(z_2) \end{bmatrix} \tag{3}$$

where $\boldsymbol{J}$ is the surface current density vector. $\overline{\boldsymbol{T}}_1$ and $\overline{\boldsymbol{T}}_2$ are the transfer matrices at, respectively, the interfaces planes: $z = z_1$ and $z = z_2$, given by the following matrix:

$$\overline{\boldsymbol{T}}_n = \begin{bmatrix} \overline{\boldsymbol{T}}_n^{11} & \overline{\boldsymbol{T}}_n^{12} \\ \overline{\boldsymbol{T}}_n^{21} & \overline{\boldsymbol{T}}_n^{22} \end{bmatrix}, n = 1, 2$$

$$\overline{\boldsymbol{T}}_n^{11} = \overline{\boldsymbol{T}}_n^{22} = \begin{bmatrix} \cos(k_{Z_n} h_n) & 0 \\ 0 & \cos(k_{Z_n} h_n) \end{bmatrix} \tag{4a}$$

$$\overline{\boldsymbol{T}}_n^{12} = \begin{bmatrix} -j\frac{k_{Z_n}}{\omega\varepsilon_n}\sin(k_{Z_n} h_n) & 0 \\ 0 & -j\frac{\omega\mu_n}{k_{Z_n}}\sin(k_{Z_n} h_n) \end{bmatrix} \tag{4b}$$

$$\overline{\boldsymbol{T}}_n^{21} = \begin{bmatrix} -j\frac{\omega\varepsilon_n}{k_{Z_n}}\sin(k_{Z_n} h_n) & 0 \\ 0 & -j\frac{k_{Z_n}}{\omega\mu_n}\sin(k_{Z_n} h_n) \end{bmatrix} \tag{4c}$$

In the unlimited region of free space, the electric field is related to the magnetic field by:

$$\tilde{\boldsymbol{H}}_3(\boldsymbol{k}_s, z_2^+) = \overline{\boldsymbol{g}}_0 \tilde{\boldsymbol{E}}_3(\boldsymbol{k}_s, z_2^+) \tag{5}$$

where

$$\overline{\mathbf{g}}_0 = \begin{bmatrix} \frac{\omega\varepsilon_0}{k_z} & 0 \\ 0 & \frac{k_z}{\omega\mu_0} \end{bmatrix} = \begin{bmatrix} \sqrt{\frac{\varepsilon_0}{\mu_0}} & 0 \\ 0 & \sqrt{\frac{\varepsilon_0}{\mu_0}} \end{bmatrix}$$

Using equations from (1) to (5), $\tilde{\boldsymbol{E}}(\boldsymbol{k}_s, z_1)$, $\tilde{\boldsymbol{E}}(\boldsymbol{k}_s, z_2)$, $\boldsymbol{J}^1(\boldsymbol{k}_s)$, and $\boldsymbol{J}^2(\boldsymbol{k}_s)$ are related to each other, by the following relations:

$$\tilde{\boldsymbol{E}}(\boldsymbol{k}_s, z_1) = \overline{\boldsymbol{G}}^{11}(\boldsymbol{k}_s)\boldsymbol{J}^1(\boldsymbol{k}_s) + \overline{\boldsymbol{G}}^{12}(\boldsymbol{k}_s)\boldsymbol{J}^2(\boldsymbol{k}_s) \tag{6a}$$

$$\tilde{\boldsymbol{E}}(\boldsymbol{k}_s, z_2) = \overline{\boldsymbol{G}}^{21}(\boldsymbol{k}_s)\boldsymbol{J}^1(\boldsymbol{k}_s) + \overline{\boldsymbol{G}}^{22}(\boldsymbol{k}_s)\boldsymbol{J}^2(\boldsymbol{k}_s) \tag{6b}$$

where $\overline{\boldsymbol{G}}^{11}(\boldsymbol{k}_s)$, $\overline{\boldsymbol{G}}^{12}(\boldsymbol{k}_s)$, $\overline{\boldsymbol{G}}^{21}(\boldsymbol{k}_s)$ and $\overline{\boldsymbol{G}}^{22}(\boldsymbol{k}_s)$ are the tensor components of the spectral Dyadic Green functions given by:

$$\overline{\boldsymbol{G}}^{11}(\boldsymbol{k}_s) = \overline{\mathbf{T}}_1^{12}\left[\overline{\mathbf{g}}_0\overline{\mathbf{T}}_2^{12} - \overline{\mathbf{T}}_2^{22}\right]\left[\overline{\mathbf{g}}_0\overline{\mathbf{T}}_2^{12} - \overline{\mathbf{T}}_2^{22}\right]^{-1} \tag{7a}$$

$$\overline{\boldsymbol{G}}^{12}(\boldsymbol{k}_s) = \overline{\boldsymbol{G}}^{21}(\boldsymbol{k}_s) = \overline{\mathbf{T}}_1^{12}\left[\overline{\mathbf{T}}_2^{22} - \overline{\mathbf{g}}_0\overline{\mathbf{T}}_2^{12}\right]^{-1} \tag{7b}$$

$$\overline{\boldsymbol{G}}^{22}(\boldsymbol{k}_s) = \left[\overline{\mathbf{T}}_1^{11}\overline{\mathbf{T}}_2^{12} + \overline{\mathbf{T}}_1^{12}\overline{\mathbf{T}}_2^{22}\right]\left[\overline{\mathbf{T}}_2^{22} - \overline{\mathbf{g}}_0\overline{\mathbf{T}}_2^{12}\right]^{-1} \tag{7c}$$

3.2 Integral equations formulation

The transverse electric field, on both of the bottom and the top patches, can be obtained, respectively, from Eqs. (6a) and (6b) via the inverse Fourier transform vector:

$$\boldsymbol{E}(\boldsymbol{r}_s, z_1) = \frac{1}{4\pi^2}\iint_{-\infty-\infty}^{+\infty+\infty} \overline{\boldsymbol{F}}(\boldsymbol{k}_s, \boldsymbol{r}_s)[\overline{\boldsymbol{G}}^{11}(\boldsymbol{k}_s)\boldsymbol{J}^1(\boldsymbol{k}_s) + \overline{\boldsymbol{G}}^{12}(\boldsymbol{k}_s)\boldsymbol{J}^2(\boldsymbol{k}_s)]\mathrm{d}k_x\mathrm{d}k_y \tag{8a}$$

$$\boldsymbol{E}(\boldsymbol{r}_s, z_2) = \frac{1}{4\pi^2}\iint_{-\infty-\infty}^{+\infty+\infty} \overline{\boldsymbol{F}}(\boldsymbol{k}_s, \boldsymbol{r}_s)[\overline{\boldsymbol{G}}^{21}(\boldsymbol{k}_s)\boldsymbol{J}^1(\boldsymbol{k}_s) + \overline{\boldsymbol{G}}^{22}(\boldsymbol{k}_s)\boldsymbol{J}^2(\boldsymbol{k}_s)]\mathrm{d}k_x\mathrm{d}k_y \tag{8b}$$

where

$$\overline{\boldsymbol{F}}(\boldsymbol{k}_s, \boldsymbol{r}_s) = \frac{1}{|\boldsymbol{k}_s|}\begin{bmatrix} k_x & k_y \\ k_y & -k_x \end{bmatrix} \mathrm{e}^{j\boldsymbol{k}_s\boldsymbol{r}_s}$$

These fields are canceled, respectively, on bottom and top patches:

$$\boldsymbol{E}(x, y, z_1) = 0 \tag{9a}$$

$$\boldsymbol{E}(x, y, z_2) = 0 \tag{9b}$$

3.3 Integral equations solution

Current density distribution, on the bottom patch, $\boldsymbol{J}^1(x, y)$, and on the top patch, $\boldsymbol{J}^2(x, y)$, are given in Eqs. (10a) and (10b) using Galerkin procedure:

$$\boldsymbol{J}^1(x, y) = \sum_{n=1}^{N} a_n \begin{bmatrix} J_{xn}^1(x, y) \\ 0 \end{bmatrix} + \sum_{m=1}^{M} b_m \begin{bmatrix} 0 \\ J_{ym}^1(x, y) \end{bmatrix} \tag{10a}$$

$$\boldsymbol{J}^2(x, y) = \sum_{p=1}^{P} c_p \begin{bmatrix} J_{xp}^2(x, y) \\ 0 \end{bmatrix} + \sum_{q=1}^{Q} d_q \begin{bmatrix} 0 \\ J_{yq}^2(x, y) \end{bmatrix} \tag{10b}$$

where J_{xn}^1, J_{ym}^1, J_{xp}^2 and J_{yq}^2 are the basic functions, and a_n, b_m, c_p, and d_q are the unknown coefficients of the modal to be determined. Using the method of moments, Eqs. (9a)

and (9b) are reduced to a linear system of homogenous equations:

$$\begin{bmatrix} \begin{bmatrix} (\overline{\boldsymbol{U}}^{11})_{N\times N} & (\overline{\boldsymbol{U}}^{12})_{N\times M} \\ (\overline{\boldsymbol{U}}^{21})_{M\times N} & (\overline{\boldsymbol{U}}^{22})_{M\times M} \end{bmatrix} & \begin{bmatrix} (\overline{\boldsymbol{V}}^{11})_{N\times P} & (\overline{\boldsymbol{V}}^{12})_{N\times Q} \\ (\overline{\boldsymbol{V}}^{21})_{M\times P} & (\overline{\boldsymbol{V}}^{22})_{M\times Q} \end{bmatrix} \\ \begin{bmatrix} (\overline{\boldsymbol{W}}^{11})_{P\times N} & (\overline{\boldsymbol{W}}^{12})_{P\times M} \\ (\overline{\boldsymbol{W}}^{21})_{Q\times N} & (\overline{\boldsymbol{W}}^{22})_{Q\times M} \end{bmatrix} & \begin{bmatrix} (\overline{\boldsymbol{Z}}^{11})_{P\times P} & (\overline{\boldsymbol{Z}}^{12})_{P\times Q} \\ (\overline{\boldsymbol{Z}}^{21})_{Q\times P} & (\overline{\boldsymbol{Z}}^{22})_{Q\times Q} \end{bmatrix} \end{bmatrix} \cdot \begin{bmatrix} (\boldsymbol{a})_{N\times 1} \\ (\boldsymbol{b})_{M\times 1} \\ (\boldsymbol{c})_{P\times 1} \\ (\boldsymbol{d})_{Q\times 1} \end{bmatrix} = 0 \tag{11}$$

To avoid the trivial solution, it is required that the determinant of its matrix must be zero:

$$det\left(\overline{\boldsymbol{\Omega}}(f)\right) = 0, \overline{\boldsymbol{\Omega}} = \begin{bmatrix} \overline{\boldsymbol{U}} & \overline{\boldsymbol{V}} \\ \overline{\boldsymbol{W}} & \overline{\boldsymbol{Z}} \end{bmatrix} \tag{12}$$

Complex resonant frequencies are the roots of Eq. (12), which help to estimate the half power fractional bandwidth given by the following equation:

$$\mathrm{BW}(\%) = \frac{2f_i}{f_r} \times 100\% \tag{13}$$

where f_r is the operating frequency; whereas, f_i is the imaginary part due to radiation losses. The inverse of the BW gives the total quality factor of the antenna, and it is as follows:

$$Q_t = \frac{1}{\mathrm{BW}} = \frac{f_r}{2f_i} \tag{14}$$

The general expression of the total quality factor is given by [20, 21]

$$\frac{1}{Q_t} = \frac{1}{Q_c} + \frac{1}{Q_d} + \frac{1}{Q_{\mathrm{sw}}} + \frac{1}{Q_{\mathrm{rad}}} \tag{15}$$

where Q_c: quality factor due to ohmic losses, Q_d: quality factor due to dielectric losses, related to DF by $\tan\delta = 1/Q_d$, Q_{sw}: quality factor due to surface waves, and Q_{rad}: quality factor due to radiation losses.

In this study, only nonmagnetic dielectric materials are considered, having the free space permeability ($\mu = \mu_0$) and complex dielectric permittivity (with dielectric losses).

An applied electric field causes the polarization of the atoms or molecules of the dielectric material, which creates electric dipole moments that increase the total displacement flux $\boldsymbol{D}$, as it is given in Eq. (16),

$$\boldsymbol{D} = \varepsilon_0 \boldsymbol{E} + \boldsymbol{P}_e = \varepsilon_0 (1 + \chi_e)\boldsymbol{E} = \varepsilon \boldsymbol{E} \tag{16}$$

where $\boldsymbol{P}_e$ is the electric polarization vector, χ_e is the complex electric susceptibility.

For lossy dielectric materials, we have:

$$\boldsymbol{J} = \sigma \boldsymbol{E} \tag{17}$$

$$\varepsilon = \varepsilon' - \mathrm{j}\varepsilon'' \tag{18}$$

with $\varepsilon' = \varepsilon_0 \varepsilon_r$, and ε'' is due to the dielectric losses. In such case, Maxwell–Ampère equation becomes:

$$\nabla \times \boldsymbol{H} = \sigma \boldsymbol{E} + j\varepsilon\omega \boldsymbol{E} = j\omega\varepsilon' \left(1 - j\frac{\sigma + \omega\varepsilon''}{\omega\varepsilon'}\right)\boldsymbol{E} \tag{19}$$

An equivalent dielectric permittivity is introduced, as it is given in the following equation:

$$\varepsilon = \varepsilon' \left(1 - j\frac{\sigma + \omega\varepsilon''}{\omega\varepsilon'}\right) = \varepsilon_0 \varepsilon_r \left(1 - j\frac{\sigma + \omega\varepsilon''}{\omega\varepsilon'}\right) \tag{20}$$

where σ is the conductivity of the dielectric material, and the ratio $\frac{\sigma+\omega\varepsilon''}{\omega\varepsilon'}$ represents DF or the so-called dielectric loss tangent ($\tan\delta$). According to Eq. (20), the wave number k within an isotropic and lossy dielectric material has the following expression:

$$k = \omega\sqrt{\mu\varepsilon} = \omega\sqrt{\mu_0\varepsilon_0\varepsilon_r}\sqrt{1 - j\tan\delta} \tag{21}$$

Since $\tan\delta$ is very low, then $\sqrt{1 - j\tan\delta} \approx 1 - \frac{1}{2}j\tan\delta$. On the other hand, $\sqrt{\mu_0\varepsilon_0} = 1/c$, and thus,

$$k = \omega\frac{\sqrt{\varepsilon_r}}{c}\left(1 - \frac{1}{2}j\tan\delta\right) \tag{22}$$

The propagation constant γ is therefore given by:

$$\gamma = jk = \alpha + j\beta = \pi\frac{\sqrt{\varepsilon_r}}{\lambda}\tan\delta + j\omega\frac{\sqrt{\varepsilon_r}}{c} \tag{23}$$

where α and β are, respectively, the attenuation constant (in Nepers/meter) and the phase propagation constant (in radians/meter). As a result, the attenuation constant α and the phase propagation constant β within a linear and isotropic dielectric material are, respectively,

$$\alpha = \pi\frac{\sqrt{\varepsilon_r}}{\lambda}\tan\delta \tag{24a}$$

$$\beta = \omega\frac{\sqrt{\varepsilon_r}}{c} \tag{24b}$$

According to the studied case, the transfer matrices mentioned previously, in Eqs. (4a), (4b), and (4c), can be expressed as a function of dielectric proprieties as follows:

$$\overline{\boldsymbol{T}}_1^{11} = \overline{\boldsymbol{T}}_1^{22} = \overline{\boldsymbol{T}}_2^{11} = \overline{\boldsymbol{T}}_2^{22} = \begin{bmatrix} \cos\left[\beta h\left(1 - \frac{1}{2}j\tan\delta\right)\right] & 0 \\ 0 & \cos\left[\beta h\left(1 - \frac{1}{2}j\tan\delta\right)\right] \end{bmatrix} \tag{25a}$$

$$\overline{\overline{T}}_1^{12} = \overline{\overline{T}}_2^{12} = \frac{\eta_0}{\sqrt{\varepsilon_r}} \times \begin{bmatrix} \frac{1-\frac{1}{2}j\tan\delta}{\tan\delta+j}\sin\left[\beta h\left(1-\frac{1}{2}j\tan\delta\right)\right] & 0 \\ 0 & \frac{1}{\frac{1}{2}\tan\delta+j}\sin\left[\beta h\left(1-\frac{1}{2}j\tan\delta\right)\right] \end{bmatrix} \tag{25b}$$

$$\overline{\overline{T}}_1^{21} = \overline{\overline{T}}_2^{21} = \frac{\sqrt{\varepsilon_r}}{\eta_0} \times \begin{bmatrix} \frac{1-j\tan\delta}{\frac{1}{2}\tan\delta+j}\sin\left[\beta h\left(1-\frac{1}{2}j\tan\delta\right)\right] & 0 \\ 0 & -\left(\frac{1}{2}\tan\delta+j\right)\sin\left[\beta h\left(1-\frac{1}{2}j\tan\delta\right)\right] \end{bmatrix} \tag{25c}$$

where $\eta_0 = \sqrt{\frac{\mu_0}{\varepsilon_0}} \approx 120\pi\Omega$: is the free space impedance.

Equations (25a), (25b), and (25c) are the transfer matrices as a function of dielectric losses within an isotropic and lossy dielectric material, having the height h, the dielectric constant ε_r, and the dielectric loss tangent tanδ. These equations are considered as a significant outcome of the current paper, where these latter are highly correlated with the dielectric material features.

4 Results and discussion

Computations have been performed on the basis of the above formulation, including method of moments, Galerkin procedure, where the mixed boundary value is reduced to a set of coupled vector integral equations by the use of vector Hankel transform. The dominant mode is considered in the present study. Our approach is validated in [22] which is based on previously measured data in [23], and good matching was demonstrated.

In this study, four substrates are considered including: FR-4 (ideal), Taconic RF-43, Getek RG200D, and FR-4 (lossy). These latter have the same dielectric constant ($\varepsilon_r = 4.3$), but they, respectively, have different dissipation factors of 0, 0.0033, 0.0106, and 0.025.

Table 1 summarizes the bandwidth, the real part, and the imaginary part of the resonant frequency, corresponding to the three configurations. The biggest variation rate, for each configuration, is the bandwidth variation rate. This is due to the slight decrease in real part of resonant frequency value, which makes the bandwidth variation bigger than the imaginary part variation.

What can be clearly seen in this table is the high variation rate of the lower bandwidth (BW_1) corresponding to the first configuration. This band increases from 0.9756% to 3.4178% by increasing DF from 0 to 0.025. An increase of 71.46% is reached. Unlike the lower bandwidth (BW_1), the upper one (BW_2) is only increased by 44.19%; from 2.9209% to 5.2337%. This is justified using the fact that the imaginary part of the lower resonance is bigger than the higher one.

The case of one isolated patch leads to the coupling elimination between patches. This elimination is translated by the decrease of upper frequency from 3.48 GHz (patches stacked) to 3.16 GHz (bottom patch isolated). As well as, a slight increase in lower frequency, from 2.44 GHz (patches stacked) to 2.45 GHz (top patch isolated), is

Table 1 Comparison between lossy FR-4 (DF = 0.025) and ideal FR-4 (DF = 0), in terms of complex frequency and bandwidth, in stacked patch geometry

Antenna configuration	Frequency and bandwidth	Dielectric materials		Variation rate (%)
		FR-4 (Ideal)	FR-4 (Lossy)	
Patches stacked	f_{i1}(MHz)	11.9171	41.7303	71.44
	f_{i2}(MHz)	50.9500	91.2254	44.15
	f_{r1}(GHz)	2.4430	2.4419	00.04
	f_{r2}(GHz)	3.4886	3.4861	00.07
	BW_1(%)	0.9756	3.4178	71.46
	BW_2(%)	2.9209	5.2337	44.19
Antenna without bottom patch	f_i(MHz)	66.3136	102.6610	35.41
	f_r(GHz)	3.1682	3.1652	00.09
	BW(%)	4.1861	6.4869	35.47
Antenna without top patch	f_i(MHz)	14.5918	44.3387	67.09
	f_r(GHz)	2.4547	2.4535	00.05
	BW(%)	1.1889	3.6143	67.11

noticed. These results confirm those presented in the literature [24]. More results, with different values of DF, are presented as curves, in Figs. 2, 3 and 4.

The dependence of both the imaginary part of resonant frequency and the bandwidth, on DF values, is clearly presented in Figs. 2 and 3 respectively. No significant difference has been found between slopes: $\Delta BW/\Delta \tan\delta$. Roughly the same slope is noticed on both the lower bandwidth (97.688) and the bandwidth of the lower patch alone (97.016). As well, approximately the same slope is also noticed on both the upper bandwidth (92.512) and the bandwidth of the upper patch alone (92.032).

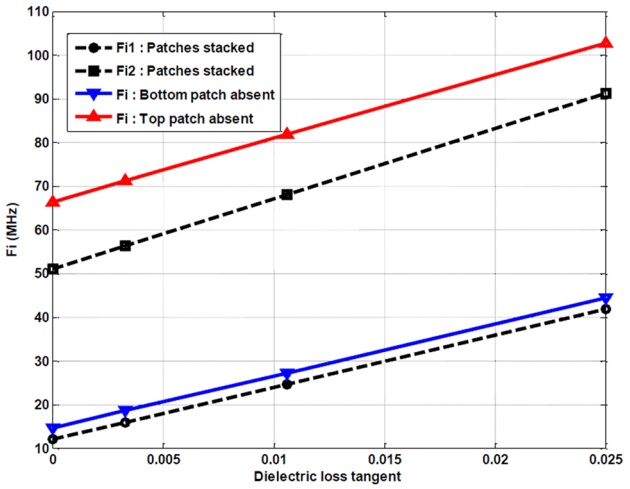

Fig. 2 Imaginary part of resonant frequency versus dielectric loss tangent corresponding to dielectric materials: FR-4 (ideal), Taconic RF-43, Getek RG200D, and FR-4 respectively

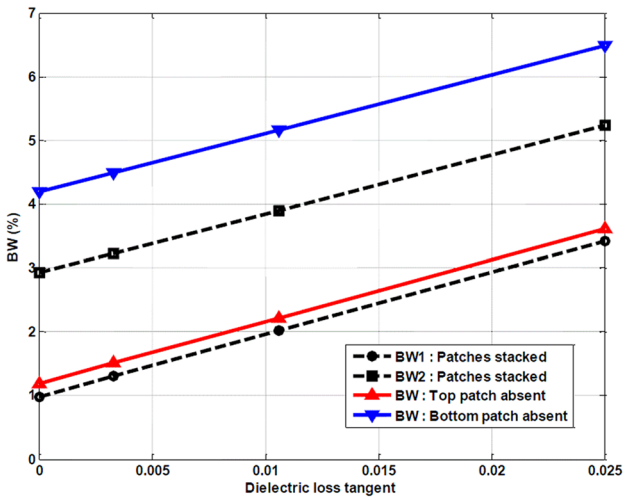

Fig. 3 Bandwidth versus dielectric loss tangent corresponding to dielectric materials: FR-4(ideal), Taconic RF-43, Getek RG200D, and FR-4 respectively

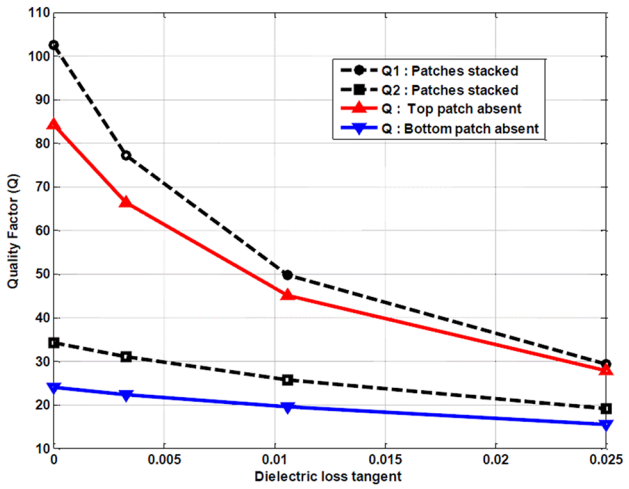

Fig. 4 Quality factor versus dielectric loss tangent corresponding to dielectric materials: FR-4 (ideal), Taconic RF-43, Getek RG200D, and FR-4 respectively

However, the two different cases show significant difference. As a result, the dependence of the bandwidth on dielectric losses becomes significant with superstrate geometry compared to the simple patch geometry.

As it is shown in Fig. 2, imaginary part of resonant frequency is significantly affected. Therefore, the bandwidth is highly correlated to dielectric losses, as it is confirmed by Fig. 3.

As presented in Fig. 4, the quality factor is negatively correlated to dielectric losses, as it is expected. No significant correlation has been found between operating frequency and dielectric losses.

5 Conclusion

A rigorous analysis of stacked rectangular patches geometry has been done, on the basis of the method of moments, Galerkin procedure. Detailed formulations are sufficiently explained with additional evidence. Transfer matrices at boundaries are given, as a function of dielectric material features, which they join both electric and magnetic fields at different interfaces. Both lower and upper bandwidths are positively affected by dielectric losses, unlike the quality factors which are negatively affected. The present study, therefore, makes several noteworthy contributions to dielectric losses analysis in stacked patch geometry. Furthermore, the paper also presents potential in modeling and analyzing dielectric losses, which has carried out significant outcomes to the antenna theory and analysis. Numerical results confirm previous findings and contribute additional evidence to the losses within nonmagnetic dielectric materials.

Compliance with ethical standards

Conflict of interest The authors declare that they have no conflict of interest.

References

1. Zhang D et al (2018) Insulation condition diagnosis of oil-immersed paper insulation based on non-linear frequency-domain dielectric response. IEEE Trans Dielectr Electr Insul 25(5):1980–1988
2. Martinez-Vega J (2010) Dielectric materials for electrical engineering. Wiley, Hoboken
3. Adams AT, Lee JK (2015) Principles of electromagnetics 2—dielectric and conductive materials. Cognella Academic Publishing, Chennai
4. Pozar DM (2012) Microwave engineering, 4th edn. Wiley, Hoboken
5. Balanis CA (2012) Advanced engineering electromagnetics, 2nd edn. Wiley, Hoboken
6. Matin MA et al (2019) Dielectric and optical properties of Ni-doped LaFeO3 nanoparticles. SN Appl Sci 1(11):1479
7. Liu J, Yang J, Zaman AU (2018) Analytical solutions to characteristic impedance and losses of inverted microstrip gap waveguide based on variational method. IEEE Trans Antennas Propag 66(12):7049–7057
8. Cavallo D (2018) Dissipation losses in artificial dielectric layers. IEEE Trans Antennas Propag 66(12):7460–7465
9. Kehn MNM, Li JY (2018) Modal analysis of corrugated plasmonic rods for the study of field localization, conductor attenuation, and dielectric losses. IEEE Trans Microw Theory Tech 66(4):1684–1700
10. Li W, Tang L, Xue F, Xin Z, Luo Z, Du G (2017) Large reduction of dielectric losses of CaCu3Ti4O12 ceramics via air quenching. Ceram Int 43(8):6618–6621
11. Bedane TF, Chen L, Marra F, Wang S (2017) Experimental study of radio frequency (RF) thawing of foods with movement on conveyor belt. J Food Eng 201(Supplement C):17–25
12. Saini A, Thakur A, Thakur P (2016) Effective permeability and miniaturization estimation of ferrite-loaded microstrip patch antenna. J Electr Mater 45(8):4162–4170
13. Nalwa HS (1999) Handbook of low and high dielectric constant materials and their applications, vol 7–2. Academic Press, Cambridge
14. E Andreou et al (2017) Magneto-dielectric substrate influence on the efficiency of a reconfigurable patch antenna. In: 2017 International workshop on antenna technology: small antennas, innovative structures, and applications (iWAT)
15. Hansen RC, Burke M (2000) Antennas with magneto-dielectrics. Microw Opt Technol Lett 26(2):75–78
16. TIkonen PM, Rozanov KN, Osipov AV, Alitalo P, Tretyakov SA (2006) Magnetodielectric substrates in antenna miniaturization: potential and limitations. IEEE Trans Antennas Propag 54(11):3391–3399
17. Niamien C, Collardey S, Sharaiha A, Mahdjoubi K (2011) Compact expressions for efficiency and bandwidth of patch antennas over lossy magneto-dielectric materials. IEEE Antennas Wirel Propag Lett 10:63–66
18. Desouky OA (2019) The effect of SiO2 addition on dielectric properties and microstructure of ZnNiO2: based ceramics. SN Appl Sci 2(1):136
19. Hasan N, Noordin NH, Karim MSA, Rejab MRM, Ma QJ (2019) Dielectric properties of epoxy–barium titanate composite for 5 GHz microstrip antenna design. SN Appl Sci 2(1):62
20. Garg R, Bhartia P, Bahl IJ, Ittipiboon A (2016) Microstrip antenna design handbook. Artech House, Norwood
21. Balanis CA (2016) Antenna theory: analysis and design, 4th edn. Wiley, Hoboken
22. B Mekimah, A Messai, S Aris, MA Meriche, T Fortaki (2014) The effect of the loss tangent on the bandwidth of the microstrip antennas in stacked configuration. In: Proceedings of 2014 mediterranean microwave symposium (MMS2014), 2014, pp 1–5
23. Couture S, Beal JC, Antar YMM (1992) Analysis of dual-frequency stacked patch antennas using subsectional bases. IEEE Microw Guided Wave Lett 2(5):185–187
24. Fortaki T, Djouane L, Chebara F, Benghalia A (2008) On the dual-frequency behavior of stacked microstrip patches. IEEE Antennas Wirel Propag Lett 7:310–313